

LAPPEENRANTA UNIVERSITY OF TECHNOLOGY

LUT School of Energy Systems

LUT Mechanical Engineering

Mohsen Amraei

EFFECTS OF FABRICATION PROCESSES ON THE BEHAVIOR OF S960 ULTRA-HIGH STRENGTH STEEL (UHSS)

Examiners: Prof. Timo Björk

M. Sc. (Tech.) Ilkka Valkonen

In memory of my Father

To my Mother

With love

ABSTRACT

Lappeenranta University of Technology
LUT School of Energy Systems
Mechanical Engineering

Mohsen Amraei

Effects of Fabrication Processes on the Behavior of S960 Ultra High Strength Steel (UHSS)

Master's thesis

2015

43 pages, 24 figures and 4 table

Examiners: Professor Timo Björk
M.Sc. (Tech.) Ilkka Valkonen

Keywords: Ultra high strength steel, fabrication processes, heat input, deformation capacity

Strenx® 960 MC is a direct quenched type of Ultra High Strength Steel (UHSS) with low carbon content. Although this material combines high strength and good ductility, it is highly sensitive towards fabrication processes. The presence of stress concentration due to structural discontinuity or notch will highlight the role of these fabrication effects on the deformation capacity of the material. Due to this, a series of tensile tests are done on both pure base material (BM) and when it has been subjected to Heat Input (HI) and Cold Forming (CF). The surface of the material was dressed by laser beam with a certain speed to study the effect of HI while the CF is done by bending the specimen to a certain angle prior to tensile test. The generated results illustrate the impact of these processes on the deformation capacity of the material, specially, when the material has HI experience due to welding or similar processes. In order to compare the results with those of numerical simulation, LS-DYNA explicit commercial package has been utilized. The generated results show an acceptable agreement between experimental and numerical simulation outcomes.

ACKNOWLEDGEMENT

Foremost, I would like to state my great sincere to my supervisor Prof. Timo Björk not only for his continuous support but also his kindness along with this thesis work.

Thanks to Mr. Ilkka Valkonen as second supervisor of this thesis work for his comments and guidelines.

I would like to take the opportunity to state my great thank to Dr. Timo Nykänen for his technical support and comments.

I would also like to appreciate the help of all members of Laboratory of Steel Structures of Lappeenranta University of Technology (LUT), especially Mr. Olli-Pekka Pynnönen and Mr. Matti Koskimäki.

The helps of Mr. Antti Heikkinen for hardness measurements and Mr. Toni Väkiparta for SEM pictures are appreciated.

I also would like to show gratitude to Factory of Future of Lappeenranta University of Technology for laser cutting and laser heating the specimens.

Financial support of SSAB, TEKES/ FIMECC is highly appreciated.

My gratitude goes to the help and support of my friends Mr. Mohammad Dabiri and Mr. Behzad Barzin for being patient and helpful not only in the scientific discussions but also their support beyond that.

Most importantly, none of this would have been possible without lovely support of my family. My immediate family who this dissertation is dedicated to, has been a great source of support, strength and love.

TABLE OF CONTENTS

ABSTRACT

ACKNOWLEDGEMENTS

TABLE OF CONTENTS

LIST OF SYMBOLS AND ABBREVIATIONS

1 INTRODUCTION	1
2 LABORATORY TESTS	3
2.1 Material Properties	3
2.2 Experimental programming	4
2.2.1 Base Material	6
2.2.2 Heat Input	9
2.2.2.1 Macro structure of heat input	9
2.2.2.2 Micro structure of heat input	11
2.2.2.3 Effects of HI on capacity of the material	12
2.2.3 Cold forming	16
2.2.3.1 Test setup	16
2.2.3.2 Cold forming effect	17
3 NUMERICAL SIMULATION AND COMPARISON BETWEEN RESULTS	21
3.1 Material Definition in LS-DYNA	21
3.2 Simulation of base material	24
3.3 Simulation with heat input effect	25
3.3.1 Fracture of specimens	26
3.3.2 Fracture through thickness	29
3.4 Simulation of cold forming effect	28
4 CONCLUSION	32
REFERENCES	33

LIST OF SYMBOLS AND ABBREVIATIONS

A_0	Original cross-section
A_d	Damaged cross-section
b	Width of specimen
D	Damage
EPPF	Effective plastic strain at which material softening begins
EPPFR	Effective plastic strain at which material ruptures
F_{max}	Maximum force
f_y	Yield stress
t	Thickness of specimen
σ_{Eng}	Engineering stress
σ_{True}	True stress
ε^p	Instant strain
ε_{Eng}	Engineering strain
ε_x	Axial strain
ε_y	Radial strain
ε_z	Tangential strain
AZ	Annealed Zone
BM	Base Material
CE	Carbon Equivalent Content
CF	Cold Forming
CGHAZ	Coarse Grain Heat Affected Zone
DP	Dual Phase
FGHAZ	Fine Grain Heat Affected Zone
FZ	Fusion Zone
HAZ	Heat Affected Zone
HI	Heat Input

HSS	High Strength Steel
ICHAZ	Inter Critical Heat Affected Zone
SCF	Stress Concentration Factor
SCHAZ	Sub Critical Heat Affected Zone
SEM	Scanning Electron Microscope
UHHS	Ultra-High Strength Steel

1 INTRODUCTION

High Strength Steels (HSS) with the minimum nominal strength of 420 MPa have different applications in various engineering sectors including construction industry and automotive (Shaw, Kuriyama & Lambriks, 2011; Matsuku, Hasegawa & Tanaka, 2007; Hasegawa, Kaneko & Seto, 2013) where an optimized combination of safety and light weight is a matter of issue (Guofei, Ming & Tau, 2012; Kawalla & Waengler, 2008). The applications of these grades of steels have been increased during the past few decades. On the other side, despite to the availability of Ultra High Strength Steels (UHSS, with nominal strengths over 890 MPa) on the market for many years, they are not commonly in use in the civil engineering industry (Wallin et al., 2015). However their applications are widely in use in different industries such as mining, agriculture, railway and especially automotive based on the combination of high strength and considerable energy absorption leading reduction of cost and weight and enhancing the safety of road issues (Azhari et al., 2015; Osawa et al., 1983; Cazes & Ronin, 2002; Nonaka et al., 2003; Mukai, 2005; Aratani et al., 2013).

There are different studies done on mechanical properties of Ultra-High Strength Steels (UHSS) (Wallin et al., 2015; Azhari et al., 2015; Guo et al., 2015), however there is a lack of scientific design rules and manufacturing experiences following a certain design standard. The specification Eurocode3 and ANSI/AISC 360-10 (2013) allows the use of high yield strength steels up to grade of S700 (700 MPa nominal yield strength) and A514 (690 MPa nominal yield strength) respectively; However, practically it is in use even for higher grade steels like S960 (minimum yield strength of 960MPa) (Wallin et al., 2015; EN 1993-1-12. 2007; Cao, Guo & Zeng, 2015). These standards are based on mild steel specifications, hence their applicability should be examined (Cao, Guo & Zeng, 2015). Unfortunately there are not many researches available in this case and still there is a gap of knowledge. For instance Turán and Horváth (2015) discusses that net section yielding cannot be confirmed by the proposed formula based on Eurocode (BS EN 1990:2002, 2002).

Due to this lack of scientific design standard for these series of steels, the behavior of the materials made of these types of steels should be investigated under different conditions. This study tries to understand the mechanical behavior of UHSS grade S960 using both laboratory tests and numerical simulations. Due to this aim, a series of tensile tests are done on the specimens with different hole-sizes consisting both pure base material and when it has been subjected to fabrication processes such as heat input (HI) and cold forming (CF). This type of steel is not tempered after hot rolling in contrast to typically used conventional quenching process where the material is tempered in different stages. In addition, CF, HI or combination of both processes are among the prominent parameters influencing mechanical properties of the material during fabrication processes. Moreover, the presence of stress concentration due to structural discontinuity or notch will highlight the role of these fabrication effects. There are different studies on the behavior of this material especially when it has been subjected to welding (Dzioba, Pała & Valkonen, 2013). Despite the good ductility of the pure base material (BM), with the presence of fabrication processes together with stress concentration results in reduction of ductility of the material. For instance, Azhari et al. (2015) discusses that the ductility of UHSS reduces after the material experiences heat.

Deformation and fracture of high-strength steels have been attracted by many researchers both experimentally and numerically (Sato et al., 2015). In the case of dynamic response of the material, the proposed methods are based on the strain rate and loading conditions. Such a method proposed by Boyce et al. (2009) using a dynamic servo hydraulic method ranging from quasi-static to dynamic loading. Modification of the original split Hopkinson method by applying newly technologies has attracted the interest of some researchers to increase the accuracy of the results (Solomos et al., 2004; Cadoni et al., 2013; Verleysen & Degrieck, 2004).

This study tries to understand the behavior of UHSS both virgin and non-virgin material experimentally and numerically. Different models are available in LS-DYNA to carry out the fracture of the material due to damage criteria such as Von Mises plasticity, the Gurson-model and enhanced Gurson by JC-failure. The current study uses the Von Mises plasticity considering damage in LS-DYNA which includes in material number 81/82. Due to this model, the damage

is defined based on the changes of the cross-section of the material with the respect to the softening and rupture strains (LS-DYNA keyword user's manual, 2015).

2 LABORATORY TESTS

In this part, it has been tried to design the test layouts to monitor the behavior of the material under static tensile tests both virgin and non-virgin plates. This should be carefully taken into account to get the most accurate results. Accordingly, the first step is to design the specimens and prepare them using the necessary laser cutting and machining processes.

2.1 Material Properties

The nominal thickness of the chosen plate is 9 mm for all the specimens coming from hot rolled strips. Chemical composition and scanning electron micrograph of the BM is shown in Table 1 and Figure 1. According to Ruukki Oy (2015), carbon equivalent (CE) of the studied material is 0.57 % for a normal plate with the thickness of more than 8 mm. The CE has been calculated based on the proposed equation (Şükrü, 2010):

$$CE = C + Mn/6 + (Cr + Mo + V)/5 + (Ni + Cu)/15 \quad (1)$$

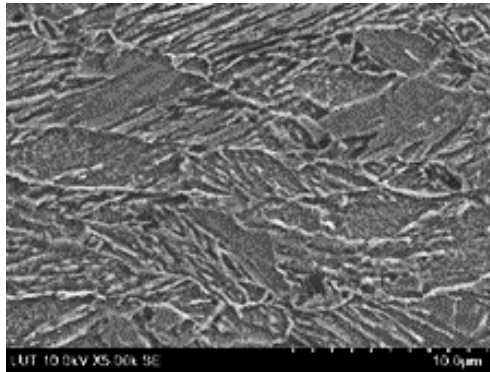


Figure 1. Scanning Electron Microscopy (SEM) of the base material.

According to Guo et al. (2015) the composition of the microstructure of BM is a mixture of tempered martensite and bainite. Since the temperature that martensite starts to establish is rather high (around 450 °C), martensite will be self-temper after transformation.

Table 1 Chemical composition of Strenx® 960 MC (wt. %) (SSAB, 2014, p. 2).

C	Si	Mn	P	S	Ti	CE
0.097	0.20	1.09	0.008	0.001	0.020	0.57

2.2 Experimental programming

The edges of the specimens are first laser cut and then machined, later the holes are made by drilling. In order to characterize the mechanic properties of the material, standard tensile tests are done in a 3 MN coupon test machine in a controlled strain rate as it has been shown in Figure 2. 3D optical measurement device capable of a frame rate of 10^3 to 10^6 per second (ARAMIS v6.3 GOM mbH) has been utilized in order to get detailed deformation of the material during the tests. It is very important to monitor local behavior of the material as the plastic strain increases during the test around the stress concentration areas, especially, the plastic deformation of non-virgin material. Calibration of the cameras are done carefully to study the deformation on the surface together with the behavior through thickness. This has been carried out by inclined view towards the specimen with the angle of 30° and sensitivity had been set to maximum in order to capture the deformation as it can be seen from Figure 2. Table 2 shows the monotonic material properties of the studied steel based on specifications by the producer and the measured values.

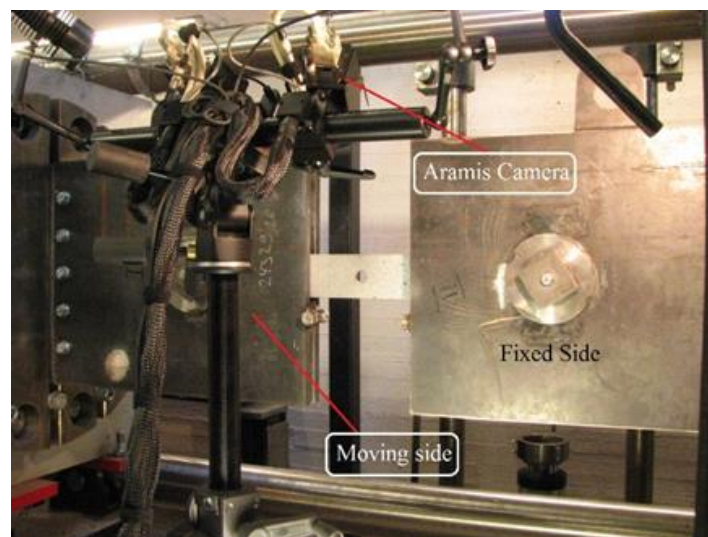


Figure 2. The 3 MN machine with installed ARAMIS used for the experimental tests.

Table 2. Mechanical properties of Strenx® 960 MC (SSAB, 2015, p. 2).

	Poison ratio	Yield stress MPa (min)	Ultimate stress (MPa)	Elongation %
Nominal	0.3	1041	1210	11
Measured	0.3	1040	1213	9

In order to carry out the laboratory tests, this investigation is divided into three different parts including:

1. Tensile tests on base material with and without hole to study the effect of stress concentration factor (SCF).
2. HI effect on the tensile properties of the material by passing a transverse laser beam on the surface of specimens.
3. Tensile tests on specimens experiencing bending to study the effect of CF.

In all the cases, there is a specimen without any hole and 3 other samples with holes in the middle consisting diameters of 8, 24 and 40 mm. Different hole-sizes result in the ratio of hole-diameter to specimen width of 0.1, 0.3 and 0.5. All the samples have the same geometry and same thickness while the hole-sizes are different which results in different stress concentration factors. The geometry of the test specimen has been designed based on EN 1993-1-12 Eurocode3 as it has been shown in Figure 3a. In order to compare the results, gauge length of 80 mm from the middle of the sample along the specimen's length has been selected for all the samples. Engineering stress-strain curve of the BM considering the specimen without any hole is shown in Figure 3b.

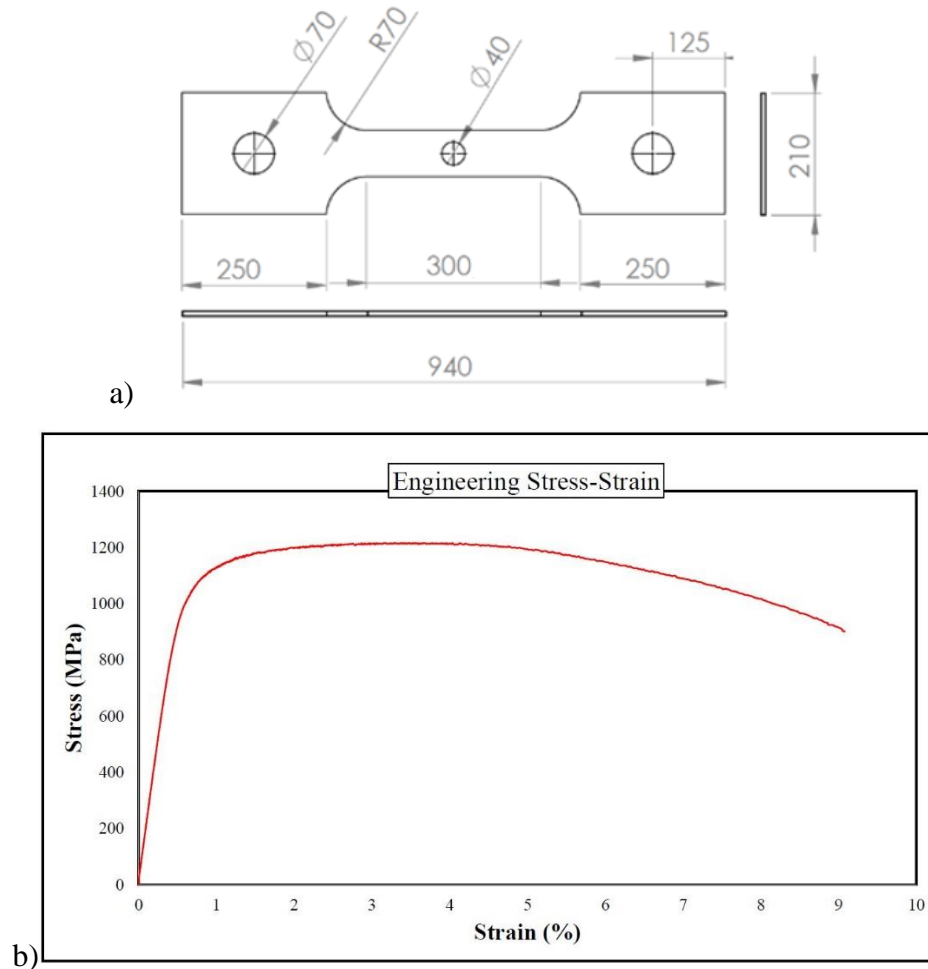


Figure 3. a) Schematic of test specimen with hole-diameter of 40 mm. b) Engineering stress-strain curve of BM without hole.

2.2.1 Base Material

For all the specimens, the surface of the material is cleaned with 6 % nitric acid solution prior to spraying the painting to capture ARAMIS pictures so that the painting remains strong enough on the surface during the test. As it can be seen from Figure 4, necking has happened for all the samples. The load-displacement curves for all the samples are shown in Figure 5. Necking causes the non-uniform longitudinal strain which leads to abrupt rupture in specimen with no hole. As it can be seen from Figure 4 when the stress is highly concentrated, hole-diameter of 8 mm, local failure around the hole starts early as the plastic strain is highly localized while the remaining cross-section is still fully under elastic tensile stress so that the force starts to drop early. However, in this case, the material still has not failed and carries more plastic

deformations till the rupture point arrives. Hence, nearly 50 % of the deformation capacity of the material is after local failure and crack initiation around the stress concentration area as it can be seen in Figure 5.

The fracture angle is followed by critical plane based on simple force balance and Von Mises yield criterion, resulted in fracture angle of 30 degree for the plate without hole. According to Björk et al. (2015) the fracture angle of a simple S960QC is around 30 degree and the maximum force is:

$$F_{max}=0.943btf_y \quad (2)$$

, where b and t are respectively width *and* thickness of the plate, f_y (MPa) is the yield strength of the material. Moreover, when the stress concentration is too high, the inclined fracture is still dominant and the material doesn't necessarily fail symmetrically perpendicular to the loading direction. It should be considered that when the hole is at its minimum, fracture angle decreases as Figure 4 shows. While the fracture is straight when the hole-diameter is 40 mm which results in ratio of diameter to width of 0.5. The straight fracture results in changing the net section of the specimens as well. Accordingly, as the hole-size decreases, the net section increases so that the fracture angle is getting steeper.

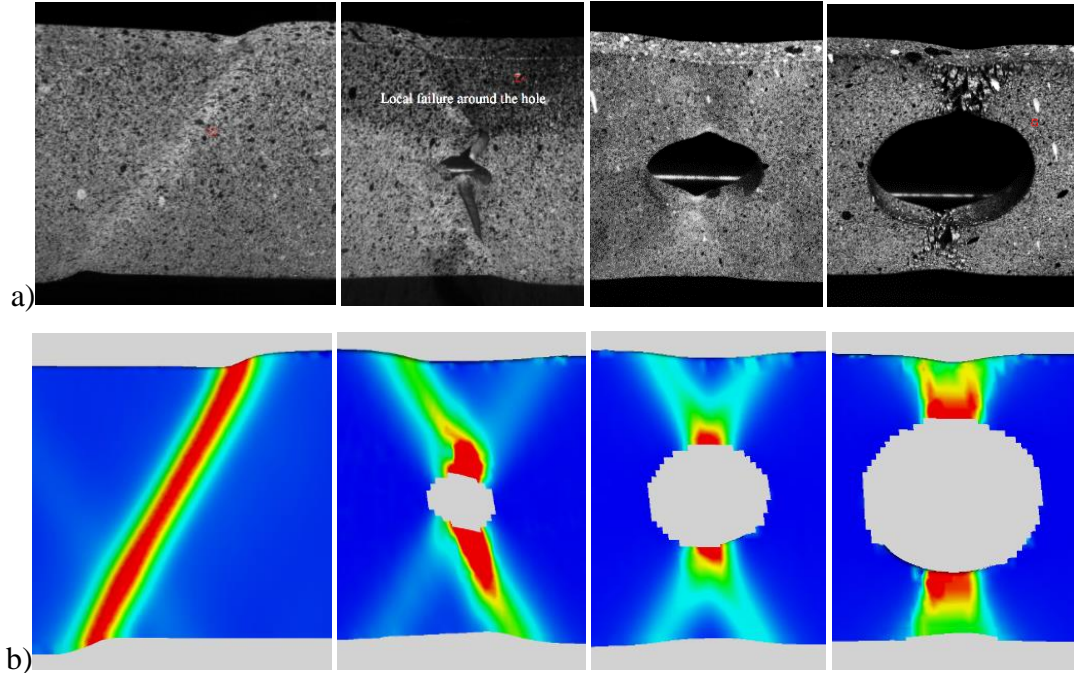


Figure 4. BM under tensile loading at the fracture point a) Test specimens, b) ARAMIS deformation contour.

The results follow the same behavior comparing to those of Turán et al. (2015) and Feldmann et al. (2015) where the net section resistance of S960 plates with the thickness of 8 mm have been studied considering different stress concentrations factors. It is possible to conclude that the inclined fracture of the plates with the thickness around 8 mm occurs when the ratio of hole-diameter to specimen width is smaller than 0.3.

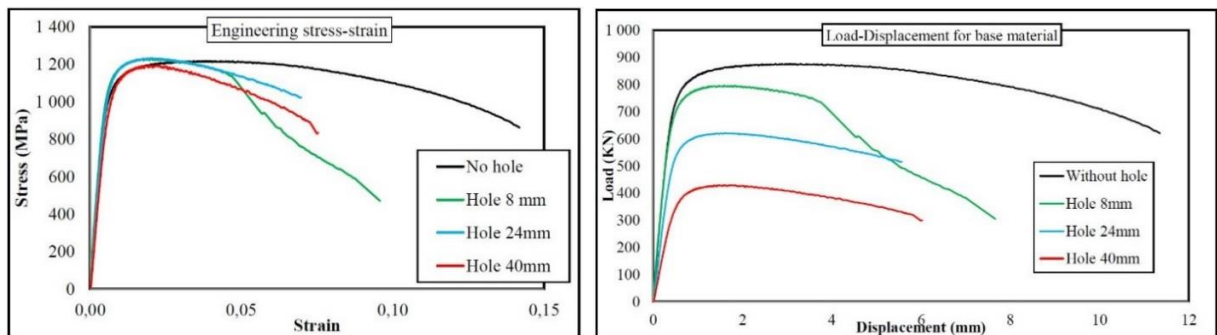


Figure 5. Engineering Stress-Strain and Force-Displacement curves in gage length of 80 mm for BM.

2.2.2 Heat Input

The second category of test specimens are considered to study the effect of local heat on the behavior of the material under tensile loading. Due to this, a laser beam generated by a 10 kW IPG fiber laser has been utilized. The applied power was 1 kW and the laser was passing on the surface of the sample with the speed of 50 mm/min. The core diameter of the optical delivery of the laser was 300 μm and the laser beam was collimated using a lens with focal length of 120 mm and focused onto the surface of the specimen by a mirror with focal length of 400 mm creating a rectangular focus spot of 4x6 mm with Rayleigh length in focus of 60 mm. Laser dressing performed on one side of the material after the holes were drilled. The beam was travelling from one edge to the other, consequently the hole-edges were stopping and starting points of heating the ligament.

Same as the previous step, there are three samples with different hole-sizes and a sample without any hole. Figure 6a shows the penetration of the heat through thickness and its distribution on the surface as well. Simple tensile coupon tests using ARAMIS to observe the behavior during the tests are done as explained before.

Micro-indentation hardness of the material after experiencing heat has been measured in different zones as Figure 6b using a Vickers micro-hardness machine (Durascan 70). The applied load and dwell period are respectively 5 kg and 10 s.

2.2.2.1 Macro structure of heat input

Macrostructure of the material after experiencing heat has been shown in Figure 7. In this case, there are four considered measurements, one consisting of a line on the top surface perpendicular to the laser beam, followed by a parallel line 10 mm under the surface through thickness, the third one is a line at the bottom of the thickness and the last one is a line along the laser beam through the surface starting from fusion zone (FZ).

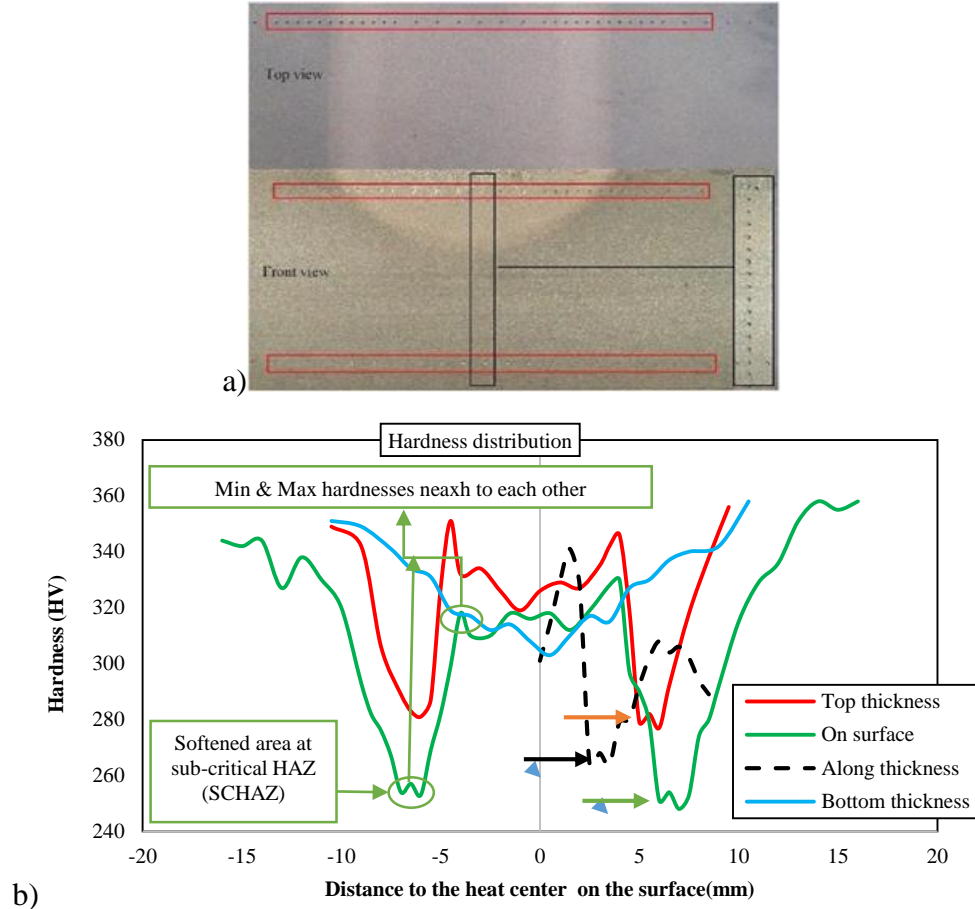


Figure 6. a) Distribution of the heat and the considered areas to measure hardness. b) Micro-hardness of the material at different zones.

The heat input reveals an elliptical shape with a smaller radius along the thickness at the beginning directly under the laser beam. However, in different subzones, the shape changes and diameters of the ellipse are going to have nearly the same dimension similar to a circular shape. This has happened because of less heat extraction throughout thickness directly under laser beam. Later, in order to carry out the finite element analysis model, the hardness distribution has been carefully taken into account. The macrostructure of the heat can be divided into four regions such as:

- Fusion Zone (FZ) in the center of heat
- Heat Affected Zone (HAZ) covers surrounding of the FZ
- Annealed Zone (AZ)
- Base Material (BM)

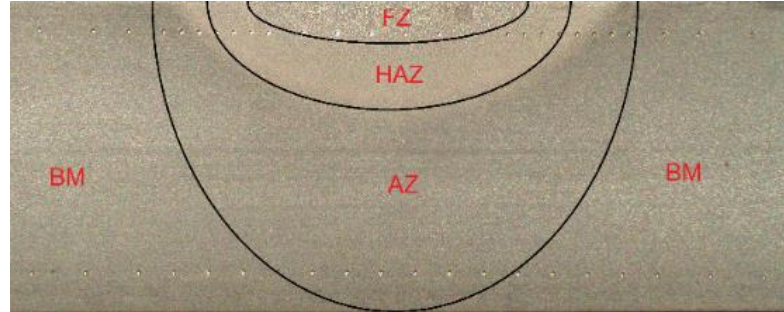


Figure 7. Macroscopic view towards thickness and different zones at the material after experiencing heat.

2.2.2.2 Micro structure of heat input

Microscopic structures of each zone has been investigated under SEM as it can be seen from figure 8. As it can be observed, the grains are bigger at FZ as they experience the maximum heat. According to Poorhaydari, Patchett and Ivey (2005) and Azhari et al. (2015), maximum temperature (- time around 1350 °C) and especially cooling rate are the key factors affecting the micro structures of welded materials. The grains are getting smaller as moving towards to the base material (distant from the laser focal point) so that the hardness of the material should increase due to Hall-Petch effect (Lyu, Ruimi & Zbib, 2015), while at some point it doesn't follow the rule of the relation between grain size and hardness. HAZ itself is a compromising of different zones according to (SSAB, 2009) and (Guo et al., 2015): Course Grain HAZ (CGHAZ), Fine Grain HAZ (FGHAZ), Inter-Critical HAZ (ICHAZ) and the Sub-Critical HAZ (SCHAZ). There is softened area at the SCHAZ as it can be seen from micro-hardness distribution where the hardness drops dramatically at the valleys. At this zone, the micro structure is similar to BM, comprising lower bainite and self-tempered martensite. Moving from HA to AZ (Annealed Zone) faces this valley located next to the point where the hardness is at its maximum excluding the BM which causes the concentration of plastic deformations at this point during the tensile test. This has happened because of phase change of the material at the softened area. During the tensile tests, for all the samples, the failure starts exactly from the border between HAZ and AZ. Even the fracture through thickness is tangential to the elliptical line between these two zones. According to Lyu et al. (2015) in the case of Dual Phase (DP) steels, the strength of the material is highly depends on the volumetric fraction of martensite phase, so that, changing this fraction leads to change in lattice friction and hardening coefficient

in the martensite phase (Lyu, Ruimi & Zbib, 2015). In the case of phase change of the material at SCHAZ from martensite to binate-martensite, since the fraction of martensite has reduced while the material does not fully change its phase, the hardness drops at this zone.

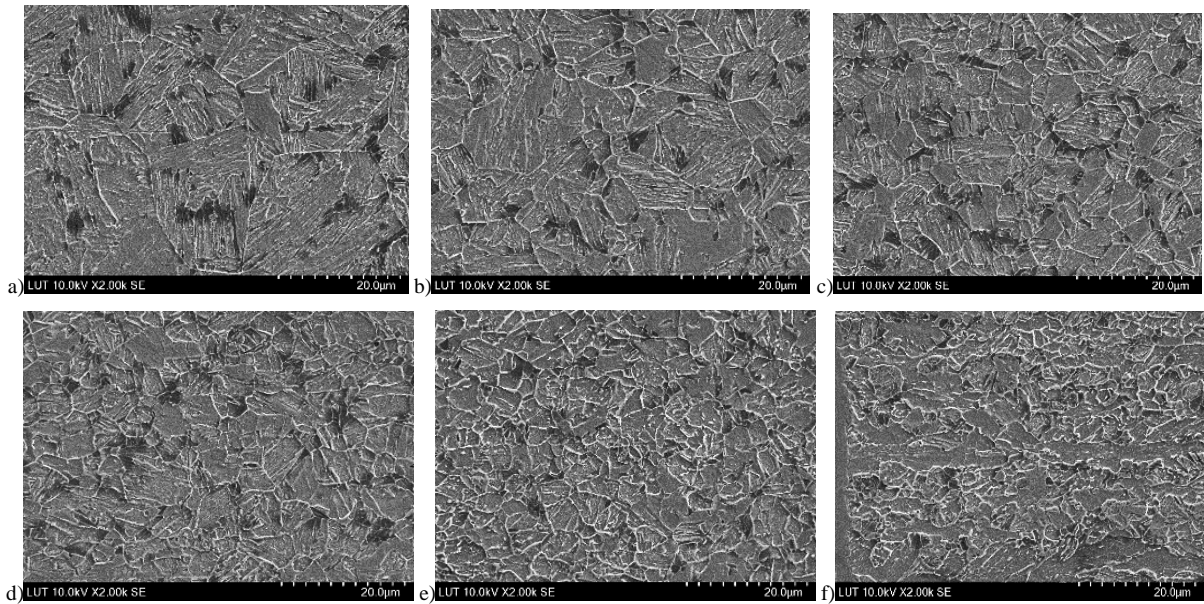


Figure 8. Micro structure of the material experiencing heat from FZ to AZ. a) FZ b) CGHAZ c) FGHAZ (Fine Grain Heat Affected Zone) d) ICHAZ (Inter Critical Heat Affected Zone) e) SCHAZ f) AZ.

2.2.2.3 Effects of HI on capacity of the material

The load displacement curves from all the tests are shown in Figure 9. With the presence of heat, the maximum load drops during the test comparing to the virgin plate is a fixed term in the range of 15.5 % in average for all the samples.

While the ultimate elongation of the specimens dramatically has reduced, specially, when there is no stress concentration. Accordingly, the specimen without hole has lost 90 % of its elongation capacity. The term relative change of deformation capacity (RCDC) has been calculated from the bellow formula:

$$RCDC = \frac{\text{Elongation of the material after treatment (mm)}}{\text{Elongation of the virgin material (mm)}} \quad (3)$$

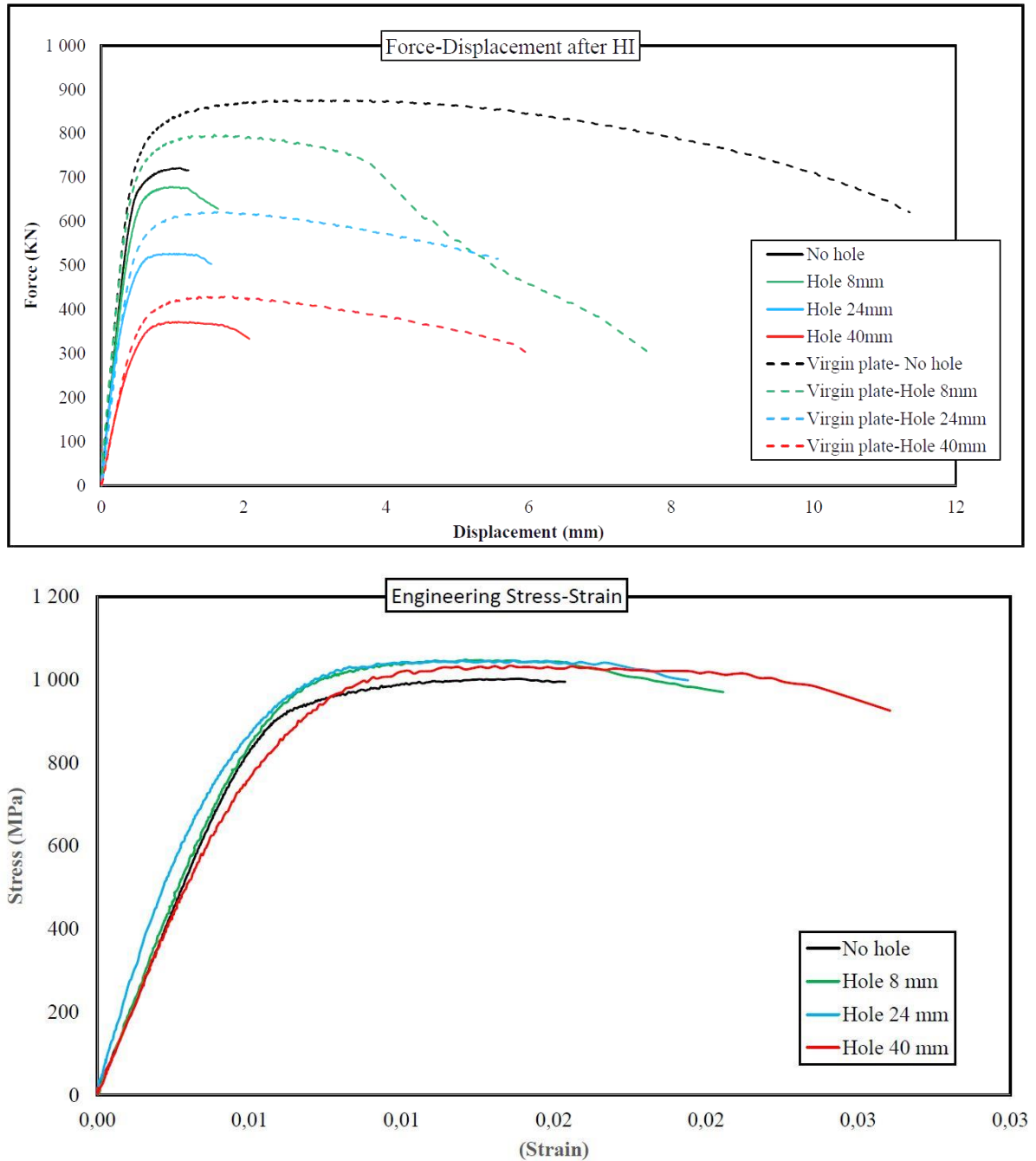


Figure 9. Force-Displacement and stress strain curves after material experienced heat.

Table 3 shows RCDC of the specimens after HI effect. As it can be seen from this table, the presence of stress concentration increases RCDC of the specimen when it has been subjected to local heat input. This has happened because of the contribution of FZ in carrying the plastic strain together with HAZ as the stress has been concentrated in this zone. In fact when there is

a hole in FZ, because of stress concentration this zone goes to necking region before HAZ fractures. The results is that the FZ which was playing a role as a constraint before having a hole in the specimen, now is contributing in carrying plastic elongation.

Table 3 Deformation capacity for different samples.

Hole diameter (mm)	0	8	24	40
Stress concentration	0	2.7	2.35	2.15
Deformation capacity	0.1	0.21	0.28	0.34

When the material is under loading at the softened area of HAZ (SCHAZ), where the hardness is at its lowest value, the difference between plastic-strain of this region comparing to surrounding areas is considerable. Based on Figure 10, the ARAMIS results says that the longitudinal strain of the elements in the SCHAZ right before the fracture point increases up to 24 % (which is an expectable behavior to be considered as softened area, ductile behavior), and at the same time the strain at the middle area is around 2 %. This difference between strains in a narrow area creates a very high stress concentration at HAZ (the maximum occurs at SCHAZ as explained before) and since UHSSs are highly susceptible towards stress concentration, crack propagation and failure of the whole material is non-negligible. Accordingly the fracture energy of the material has decreased because of experiencing heat and this results in abrupt failure of whole plate. It should be considered that the heat affected area itself shows a nearly ductile behavior as it carries the strain of 24 %. But since this is a very narrow area (nearly 2 mm) it doesn't take into account comparing the whole specimen.

When there is a stress concentration, there is a broader area under plastic deformation which causes a more homogeneous distribution of plastic strain at the critical region (SCHAZ) as it can be seen from Figure 10 and 11 (the plastic strain has been distributed from FZ to AZ consisting of all the sub zones as well). In fact, the presence of stress concentration causes the FZ contribute in carrying the plastic deformation before rupture point arrives. Consequently, the reduction of the RCDC of the specimen declines as it has been demonstrated at table 3.

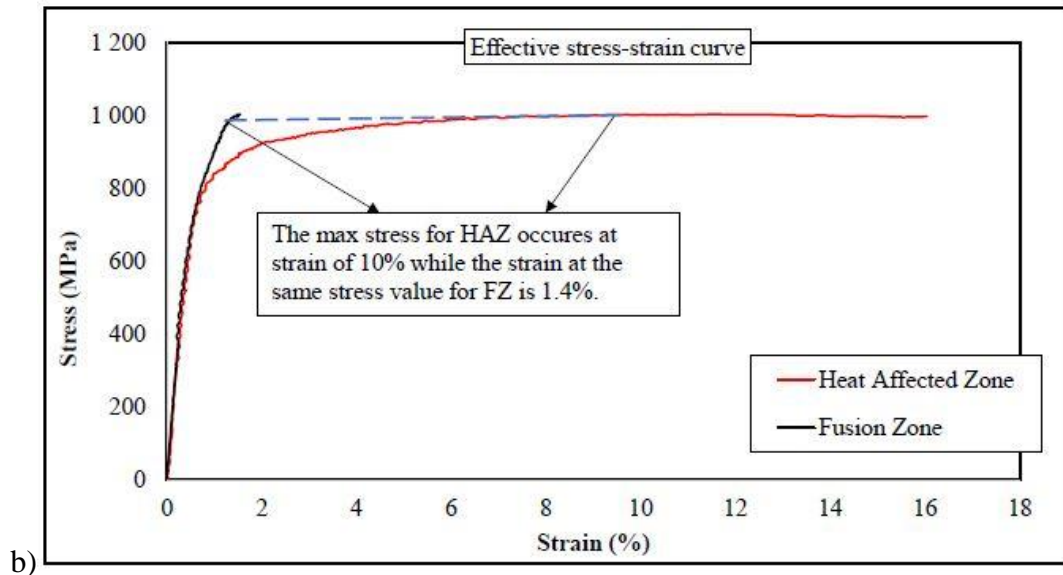
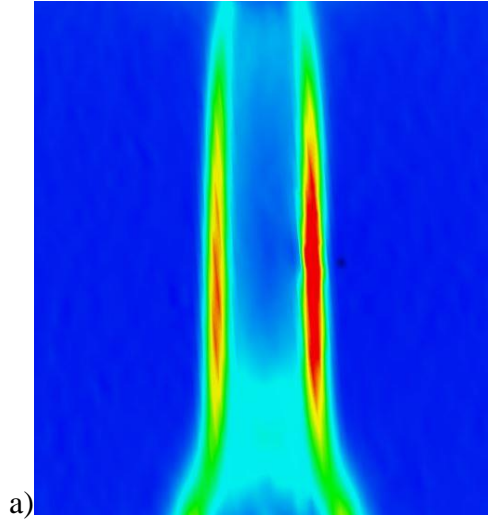


Figure 10. ARAMIS results for the specimen without hole. a) Plastic strain distribution at the failure point. b) Effective stress-strain curves till 16 % strain of HAZ.

It should be taken into account that different hole-sizes create stress concentration in different regions as it can be seen from Figure 11. For instance, when the hole-diameter is on its minimum (8 mm), however the stress is highly concentrated in FZ, the cracks start to form at SCHAZ (the border between HAZ and AZ) where there is a distance from the hole itself. With the presence of HI on the other hand, when the diameter of the hole is in the maximum (40 mm) the stress has been distributed in a broader area, accordingly the cracks start to form in a broad region. This change of moving the concentration of stress (plastic deformation) results that a broader

area of the material being under plastic deformation. Consequently, the material carries more plastic deformation till the rupture point arrives. Accordingly, when the material is subjected to HI, the presence of stress concentration results in ductile fracture of the material as it has been proven by Figure 9 as well.

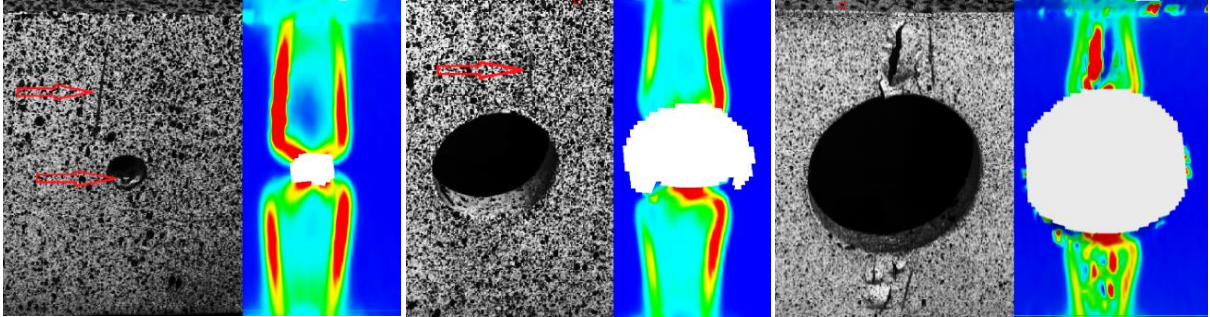


Figure 11. Distribution of strain right before fracture point (Cracks are pointed with array). Sample with hole of a) 8 mm b) 24 mm c) 40 mm.

2.2.3 Cold forming

This part is dedicated to understand how the presence of stress concentration reveals the changes in the deformation capacity of the material when it has been subjected to CF. Accordingly, some bending tests are done in advance to affect the material as CF effect prior to tensile tests.

2.2.3.1 Test setup

In order to study the effect of CF on the material behavior, the specimens are bent for 65° , then they have bent back to their original position as illustrated in Figure 12. So that the CF created a tensile residual stress in one side with compression plastic strains, and stresses opposite in sign on the other side of the plate. Then the simple coupon tensile test is done same as previous steps. The holes are drilled prior to bending the specimens. After the bending has done, the tensile test was carried out like in previous cases.

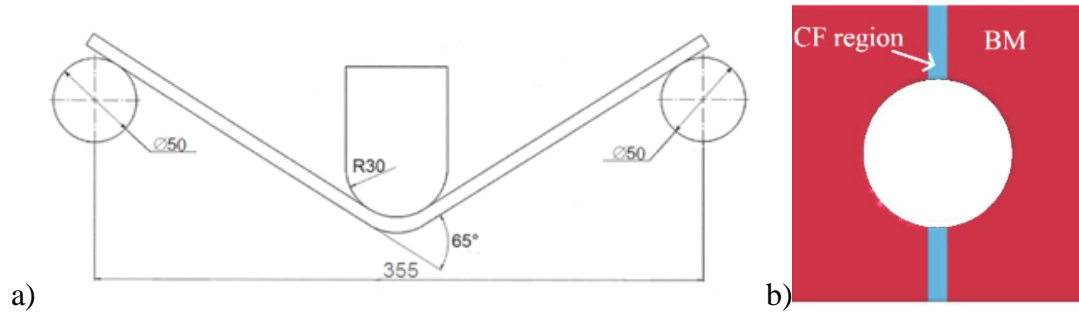


Figure 12. a) Bending procedure to study the effect of cold forming on the behavior of the material. b) CF specimen.

2.2.3.2 Cold forming effect

The generated load-displacement curves have been compared together, also with the virgin material as it has been shown in Figure 13. For all the test specimens, the maximum force drops 4.65 % in average which is significantly less change comparing to that of HI which was 15.5 %. Necking is seen for all the samples as it is observable in Figure 14. As it can be seen, when there is no stress concentration on the plate, the total elongation before fracture is in a closer range comparing that of virgin material, while under the same situation with the presence of stress concentration RCDC has dropped as Figure 13 shows.

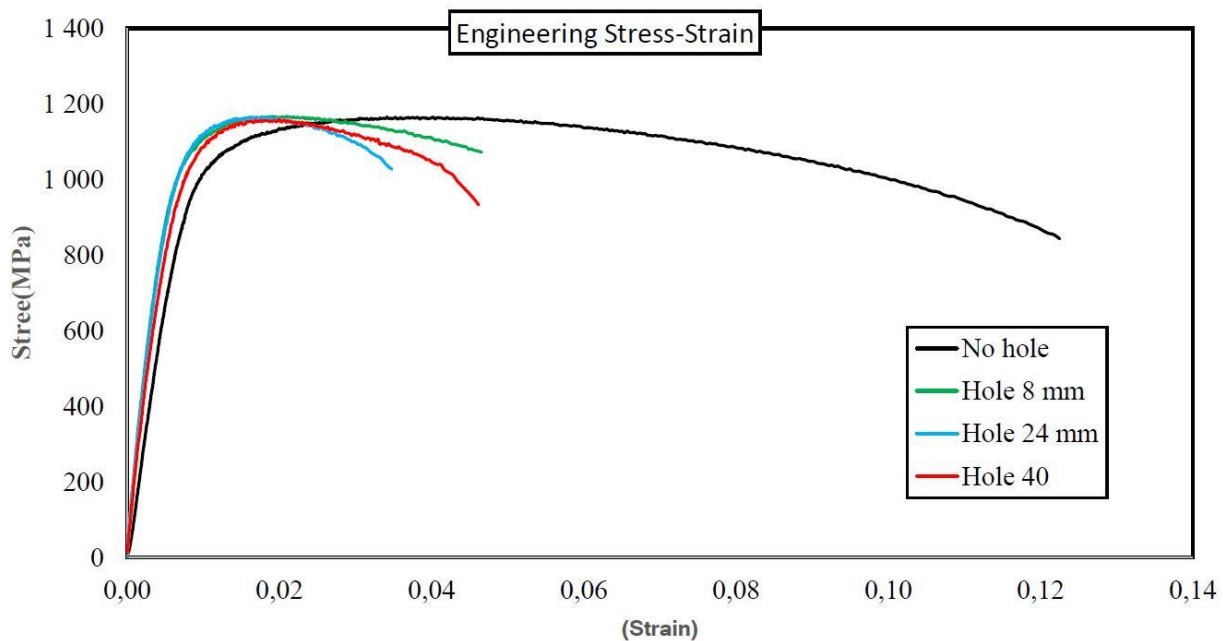
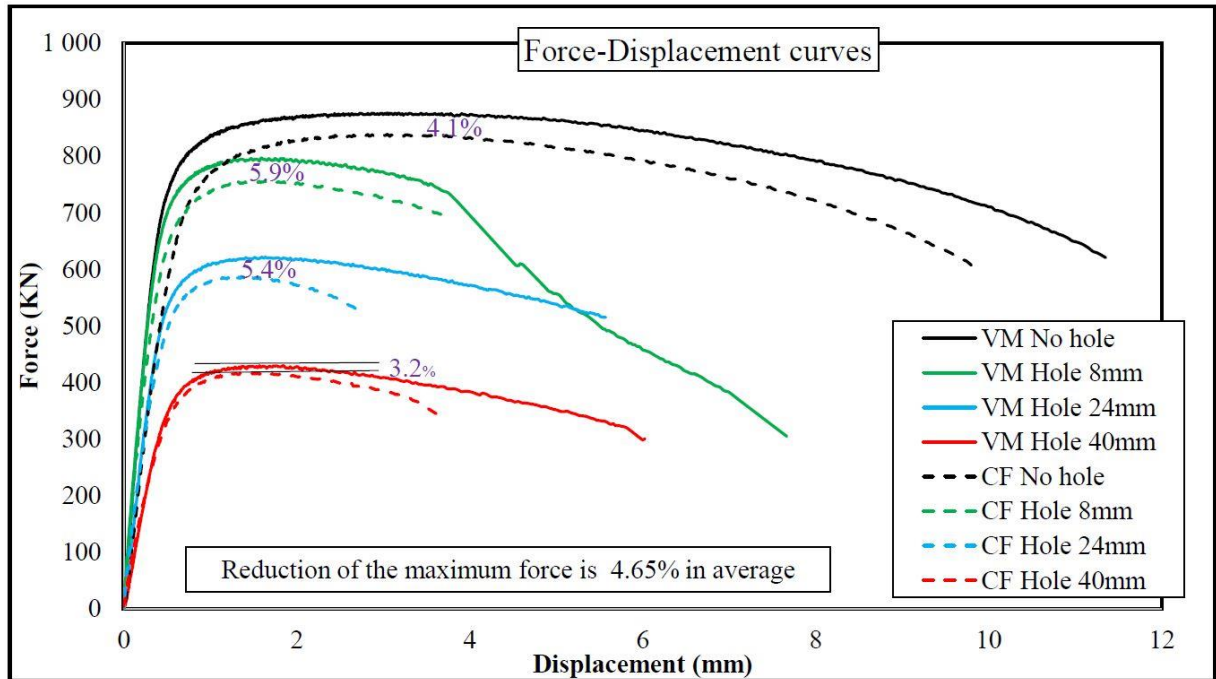


Figure 13. Load-Displacement and stress-strain curves after CF effect and the virgin material.

As it is observable from Figure 23, the less changes in deformation capacity of the material comparing to the virgin plate occurs when there is no stress concentration in the plate, holes in this case. Accordingly, when the hole-size increases which results in decreasing the stress

concentration factor, the material performance is going to be close to that of base plate without CF effect. However it should be considered that cold forming the plate weakens the material in all the cases. As it can be seen from Figure 14, experiments say that the fracture of specimens start from the CF region when there is stress concentration, while inclined fracture is a dominant when there was no stress concentration on the specimen.

In the case of virgin material, when the stress concentration is at its maximum such as the specimen with hole 8 mm, the local plastic deformation around the hole causes the failure of the material in that region, while the rest of the width is not affected so much, this causes the material show more ductility till the rupture point arrives. While for the case of hole 24 mm, it seems that the rest of the width doesn't contribute enough in carrying the strains. For the hole 40 mm, since the stress concentration is the minimum, it results in carrying more plastic deformation comparing to other specimens with stress concentration. This makes a situation where the hole 24 mm shows the weakest behavior from the point of view of displacement and strain. In all the cases, when they have also been subjected to cold forming, the combination with high stress concentration results early failure of the material.

As it can be seen from Figure 13, CF decreases the elastic modulus of the material. With the reduction of hole-size, the decreasing of the young modulus increases. Accordingly, when there is no stress concentration on the material, CF the specimen makes it more softened. It is possible to say that the effect of CF reveals itself more when there is a stress concentration in the material. Based on this, the RCDC of the material and its relation to stress concentration has been show in Table 4 calculated based on formula (2).

Table 4. Deformation capacity for different samples after CF effect.

Hole diameter (mm)	0	8	24	40
Stress concentration	0	2.7	2.35	2.15
RCDC	0.85	0.48	0.49	0.61

After CF the specimen, with the reduction of stress concentration, RCDC has increased. This is in-line with the decreasing the modulus elasticity of the material as explained before. The behavior of the specimen is affected due to stress concentration and triaxiality stress, accordingly the effective strain limit is different as the smallest and the bigger hole reduce RCDC of the plate 52 % and 39 % respectively.

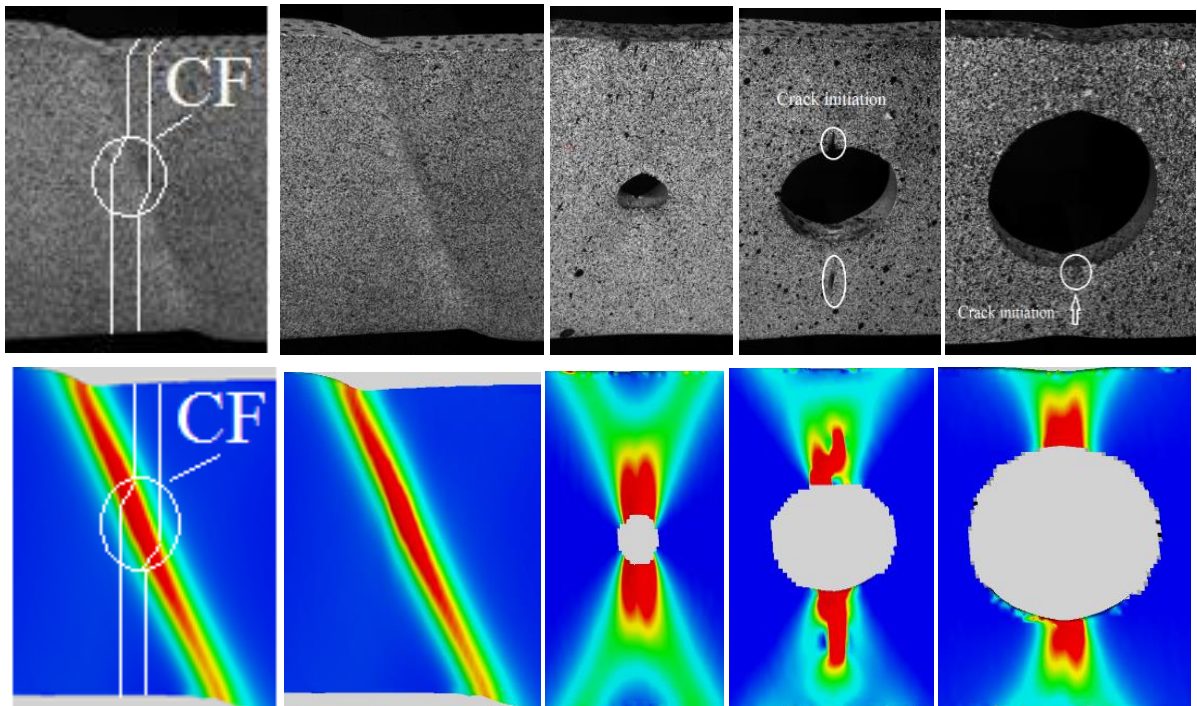


Figure 14. The specimens right before the fracture point including ARAMIS results.

3 NUMERICAL SIMULATION AND COMPARISON BETWEEN RESULTS

LS-DYNA is a very powerful software to simulate different phenomenon in mechanical engineering from static to dynamic and high strain rate applications. The explicit numerical simulation of this software attracts the major interest of engineers. The following part is dedicated to simulate all the tests that were performed at the laboratory and compare the results with those of explicit numerical simulation results.

3.1 Material Definition in LS-DYNA

The simulation is done using LS-DYNA finite element commercial package with explicit time integration. In order to carry out the numerical simulation analysis, material type 81 which according to LS-DYNA keyword user's manual (2014) is named as "MAT_PLASTICITY_WITH_DAMAGE_ORTHO" which is an "elasto-visco-plastic material with an arbitrary stress versus strain curve and arbitrary strain rate dependency" which has isotropic hardening and damage is chosen. The failure in this model is defined either based on strain in which material fails or the minimum time step size needed for element deletion. In order to define the material behavior, it is either possible to define effective stress vs true strain curve or using multi-linear curves.

The engineering stress-strain curve has been obtained from ARAMIS camera during tensile test. In order to simulate the material behavior, LS-DYNA needs the effective strain-plastic deformation curve of the element under the maximum plastic deformation. Since the plastic deformation calculated by ARAMIS is from the 2D measurement, considering the Poisson's ratio the strain at the 3rd direction has been calculated. Accordingly, the 2D strain is directed to 3D state based on von Mises formula for strain:

$$\varepsilon = \sqrt{2/3(\varepsilon_X^2 + \varepsilon_Y^2 + \varepsilon_Z^2)} \quad (4)$$

The terms ε_X , ε_Y and ε_Z are plastic strains of the element in different directions which is under the maximum strain and fails at the rupture point. The true stress is obtained from:

$$\sigma_{True} = \sigma_{Eng}(1 + \varepsilon_{Eng}) \quad (5)$$

Where ε_{Eng} is the strain of the specimen. According to LS-DYNA, ductile damage (D) has been considered by the following equations:

$$D = \frac{A_d}{A_0} \quad \text{With} \quad 1.0 \geq D \geq 0.0 \quad (6)$$

Where D is a scalar value and A_d and A_0 are the reduced and original cross section of the specimen at the necking area. Moreover, the damage has been related to the plastic strains at which softening of the elements start and end with the following equation:

$$D = \frac{\varepsilon^p - EPPF}{EPPFR - EPPF} \quad (7)$$

Where ε^p is the effective plastic strain after failure started, $EPPF$ is, according to LS-DYNA keyword user's manual (2014) "effective plastic strain at which material softening begins" and $EPPFR$ is the effective "plastic strain at which material ruptures". In sake of comparison with experimental results, same mesh size as ARAMIS has been utilized. In the case of base material, the effective stress-plastic deformation applied for the critical element considering damage criteria has been calculated as it can be seen from Figure 15. This has been generated from the base material test specimen when there is no stress concentration on the material. For all the cases when there is base material, this curve has been used. It has to be taken into account that the failure of the elements are defined as the last strain that ARAMIS shows and after that the whole part is failed. This point is considered to be the starting point of softening or $EPPF$.

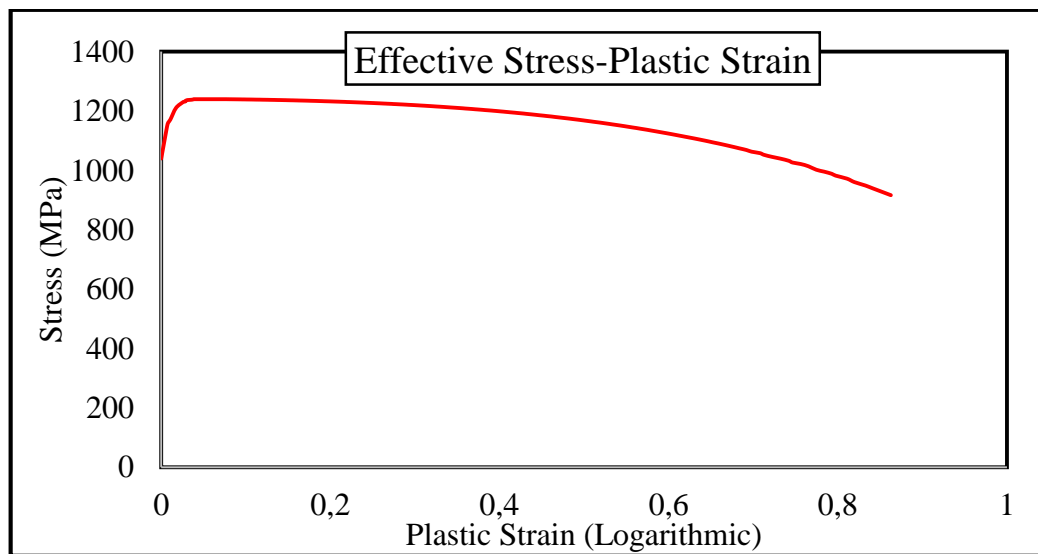


Figure 15. Effective stress-plastic deformation used for the BM.

3.2 Simulation of base material

It has to be taken into account that the failure of the elements are defined as the last strain that ARAMIS shows and after that the whole part is failed. This point is considered to be the starting point of softening or EPPF. Figure 16. Shows the load-displacement curves when there is no fabrication processes or HI and the BM itself has been studied.

As it can be seen from figure 16, when the stress concentration in the material is high, hole-diameter of 8 mm, as explained before, local failure around the hole causes the abrupt reduction of the force. Macroscopic fracture of the BM from both experiments and FEM are shown in Figure 17.

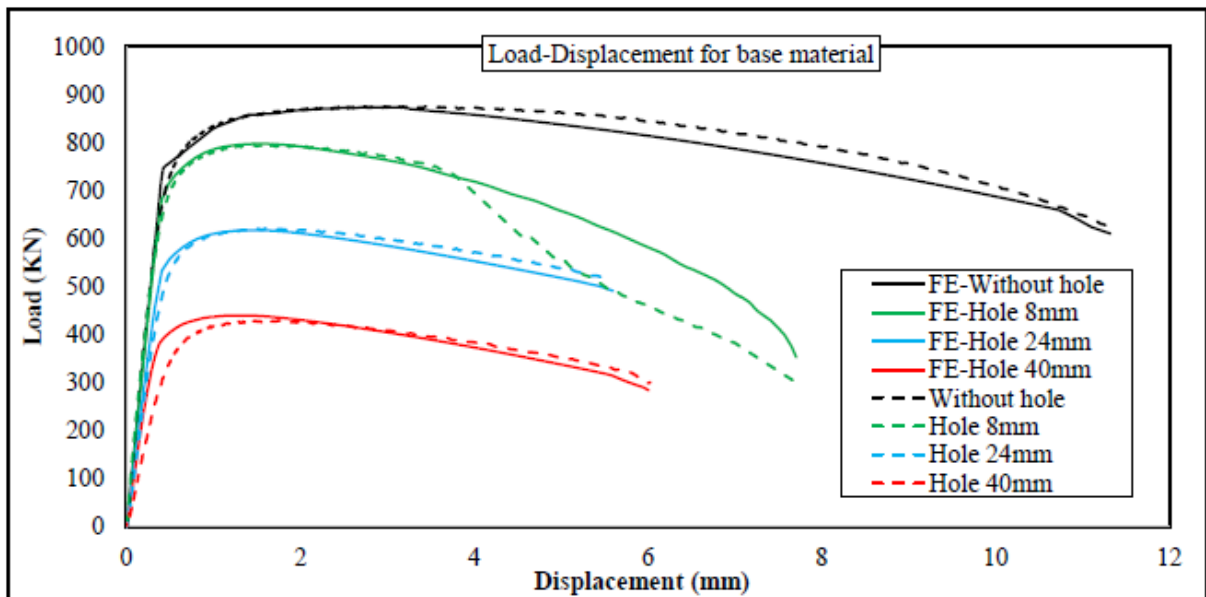


Figure 16. Load-Displacement curves for BM.

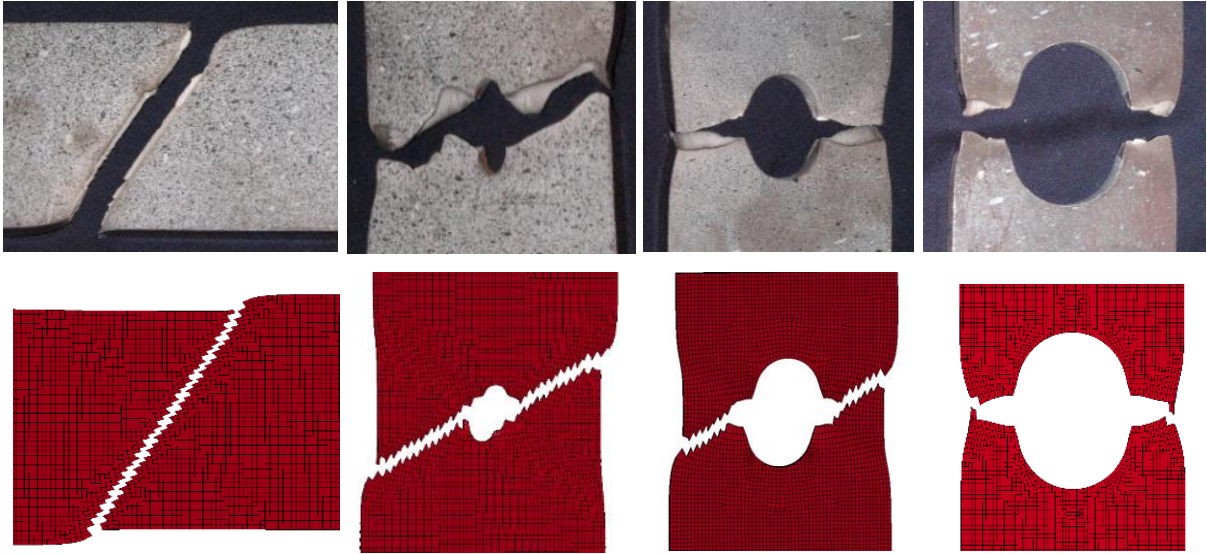


Figure 17. Macroscopic fracture of the BM from both experimental and FE.

3.3 Simulation with heat input effect

For the case of heat input, besides the ARAMIS results, hardness measurements have been considered as well. Since it is not possible to get the exact material properties and there is a lack of information how each sub-zone behaves exactly, simplifying the model is based on the assumption that all the four zones follow the same trend as the material itself has a history except the yield and ultimate stresses. This has been proven by ARAMIS as well, as it can be seen from Figure 10b. However in reality there are differences, but in this case since the fracture happens when one part (in this case HAZ) is at the latest stages of plastic deformation before rupture point arrives while other parts are at the beginning of yielding and they are experiencing just a bit of plastic deformation right after yield stress, the difference is negligible. This has been proven after the simulation was done as well.

The heat distribution on the surface is different comparing to that of penetrating through thickness, consequently the material behavior is different for both of the cases. Since it is not possible to define a very inhomogeneous material behavior for each zone, the assumption is that the minimum values from hardness measurements have been considered as the failure starts from the weakest part. This has been proven by hardness measurement from different zones and monitoring the behavior by ARAMIS. Compromising all the hardness measurements, the heat

distribution is in a way that the heat creates an elliptical shape for the FZ while the diameters of the elliptical are going to be the same size as of moving to BM similar to Figure 7. This has happened because of differences between cooling rates at various directions.

3.3.1 Fracture of specimens

As it has been mentioned before, when the material experiences HI, the fracture starts from the border between HAZ and AZ where it is called SCHAZ. This has been proven by both experimental test and FE simulation. Figure 18 shows the distribution of plastic deformations on the material right before the rupture point. Force-displacement curves generated after the HI has shown in Figure 19.

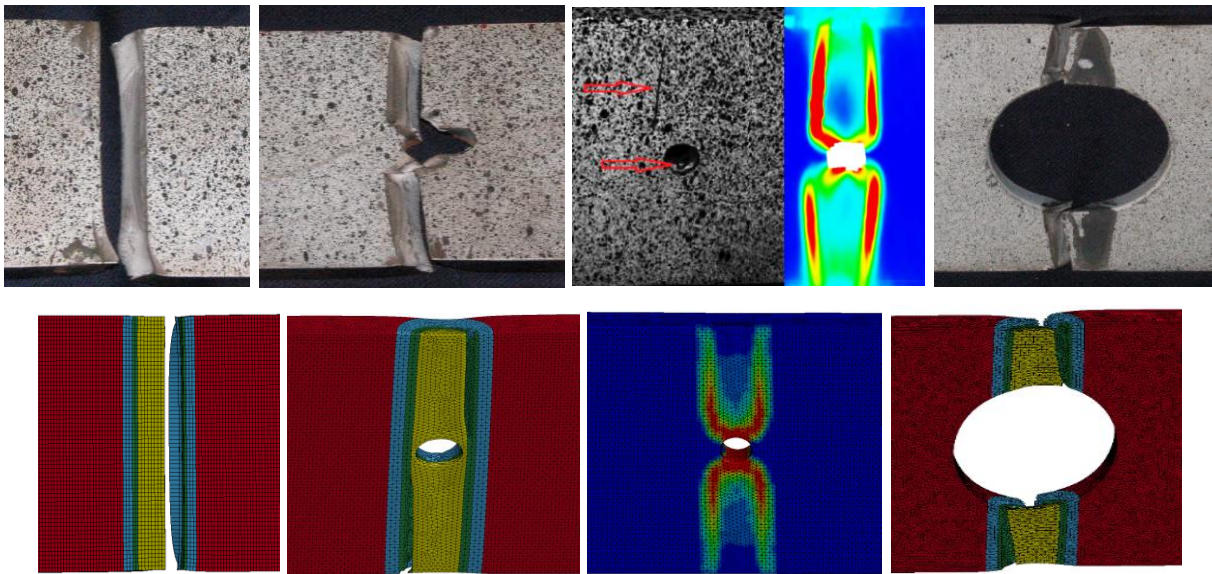


Figure 18. Macroscopic fracture of the material after experiencing HI from both experimental and FE.

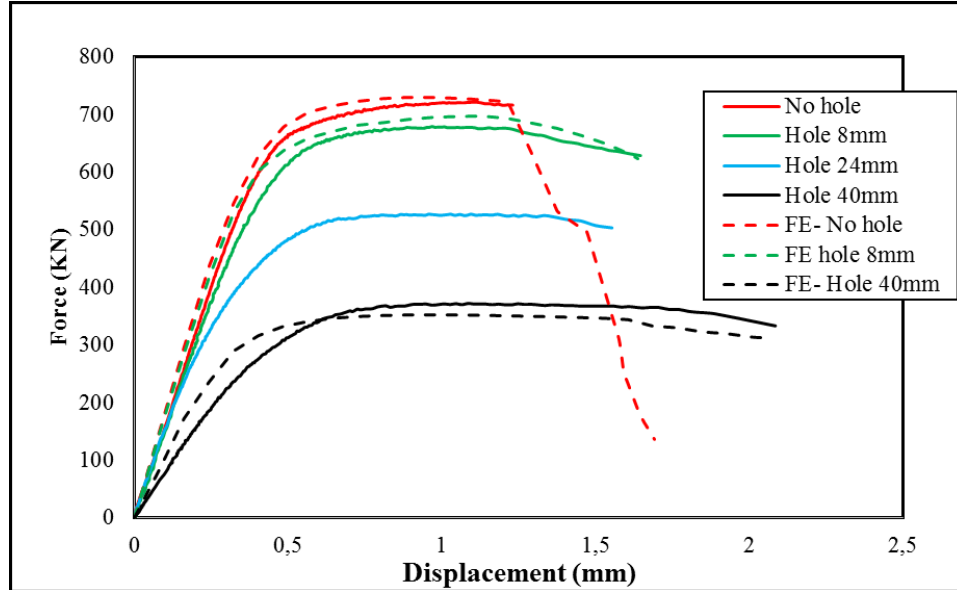


Figure 19. Force-Displacement curves for HI and cold formed samples.

Fracture surfaces of specimens after experiencing heat are shown in Figure 20. As it can be seen, the material doesn't show that much necking after HI. However in the case of pure BM, ductility of the material results in a considerable thickness reduction and plastic deformations.



Figure 20. Fracture surfaces of the material, the first row is for BM and the lower one is after experiencing HI.

Fracture surfaces of specimens after experiencing heat are shown in Figure 20. As it can be seen, the material doesn't show that much necking after HI. However in the case of pure BM, ductility of the material results in a considerable thickness reduction and plastic deformations.

of the material results in a considerable thickness reduction and plastic deformations. Yet ductile fracture at the surface of the material is seen after HI when the micro structure is seen under SEM, as Figure 21. With the presence of hole, an area with ductile fracture consisting dimples is seen at the micro structure of fracture where the stress has been concentrated. Because of high stress gradient at this region, the material goes through plastic deformation together with HAF where that area is at its weakest point. However, since the stress drops immediately as it goes far from notch tip, this region is not big enough to carry more plastic deformation before rupture point arrives for HAZ. Increasing the hole-size, makes the stress gradient less steep so that the plastic deformation (ductile fracture) distributes homogeneously in a wider region.

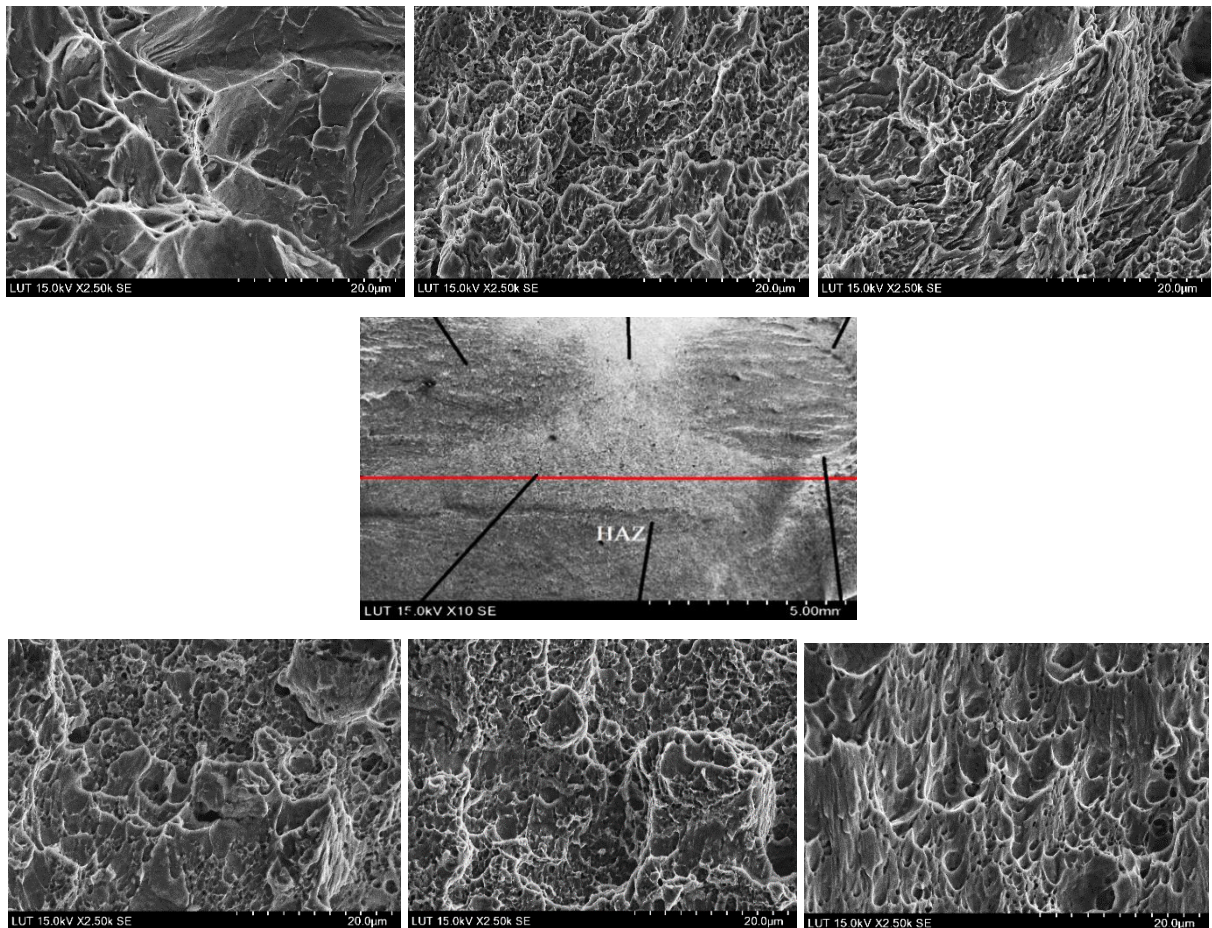


Figure 21. SEM view of the fracture surface of the material after experiencing heat with hole of 40 mm.

This results in increasing the plastic deformation capacity of the material as it has been proven by Table 3. As Figure 21 shows, the only area that shows brittle fracture (cleavage pattern) is the top left picture where it has the distance from hole together with staying far from heating zone. It also should be considered that however the voids are formed and they have been growing by the further plastic strain resulting formation of dimples, they haven't been totally gone through the maximum deformation capacity of the material as of the reduction of deformation capacity at SCHAZ.

3.3.2 Fracture through thickness

Inclined fracture through thickness is seen so that the crack starts from HAZ and propagate to other side of the plate where it is the end of AZ. As it can be seen from Figure 22, both FE and ARAMIS show the starting point of fracture at HAZ and the inclined growth through thickness leading fracture angle around 30° .

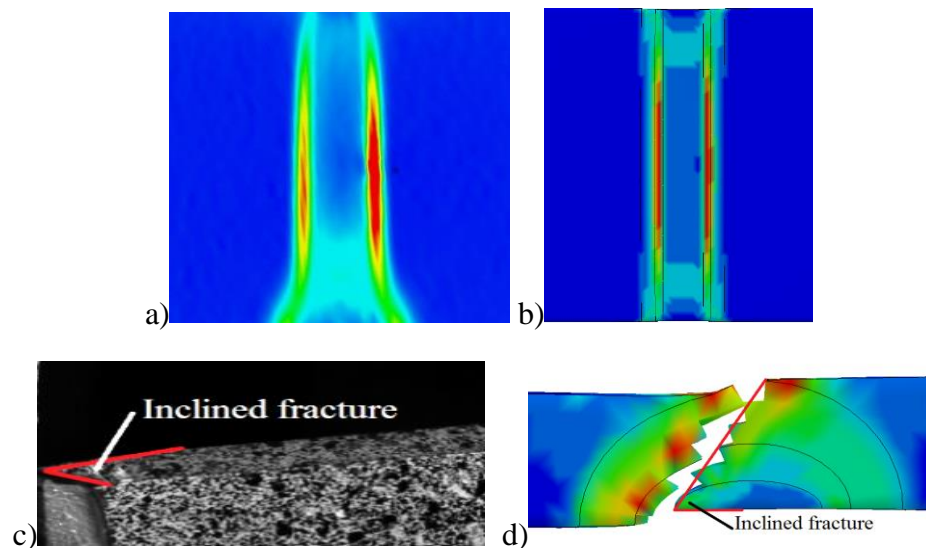


Figure 22. Aramis vs FE results when after experiencing heat without hole. a) ARAMIS b) FE c) Specimen d) FE thickness view

3.4 Simulation of cold forming effect

In order to simulate the effect of CF on the behavior of the material, the same approach has been utilized. In this case, the material has been divided in two different zones including the base

material and the CF area. Different effective stress-plastic strain curves have been applied to each zone. For all the cases, the mesh size has been calibrated with that of ARAMIS so that there is no mesh size effect on the simulation results. In this case, the curve for CF zone is defined based on the ARAMIS results when the simple plate is subjected to CF. For all the simulations, when there is a CF zone, this curve has been applied.

When the material has been cold formed, presence of stress concentration reveals the effect of the fabrication process more as the gradient of stress increases. So that, when the stress is at its maximum concentration, the material losses its deformation capacity more comparing to when the stress gradient has been distributed more smoothly. When there is no stress concentration, dominant inclined fracture resulting in increasing the net section of the fracture. However, the cold formed area carries more plastic deformation before rupture point as it has been demonstrated from both FE and experimental tests as illustrated in Figure 23 and 24.

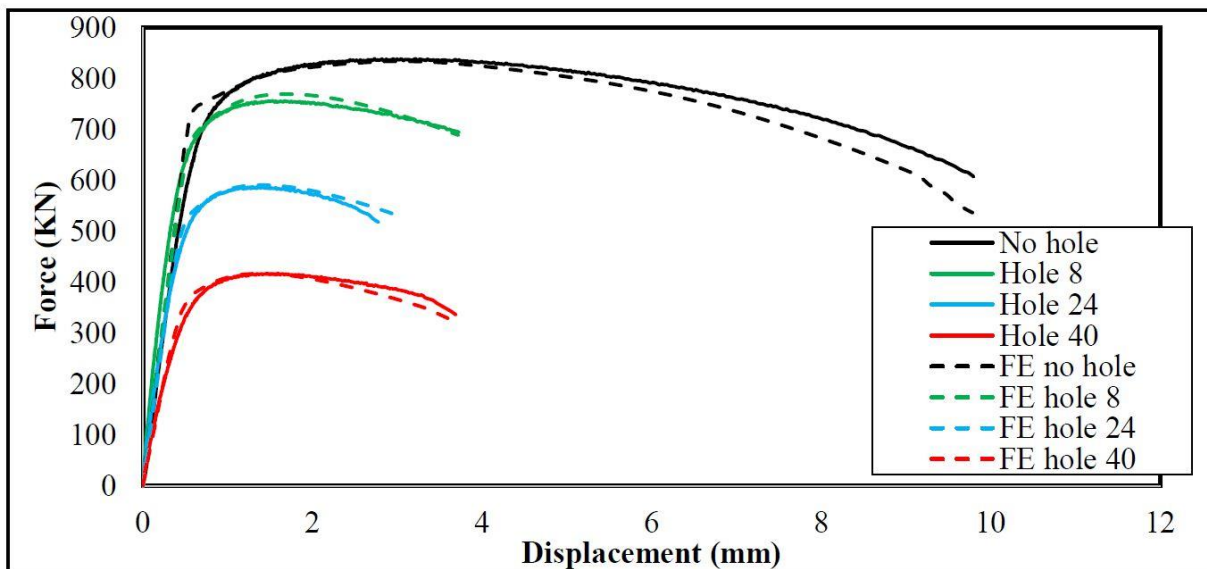


Figure 23. FE and laboratory tests of CF effect.

As it can be seen from figure 24, the fracture has started from the cold formed area as it is the weakest part due to CF effect. However, both FE and laboratory tests demonstrate that the inclined fracture of the specimen without hole is non-negligible. Accordingly, the net section

area increases in this case while it doesn't change for other cases when there is a stress concentration on the specimen.

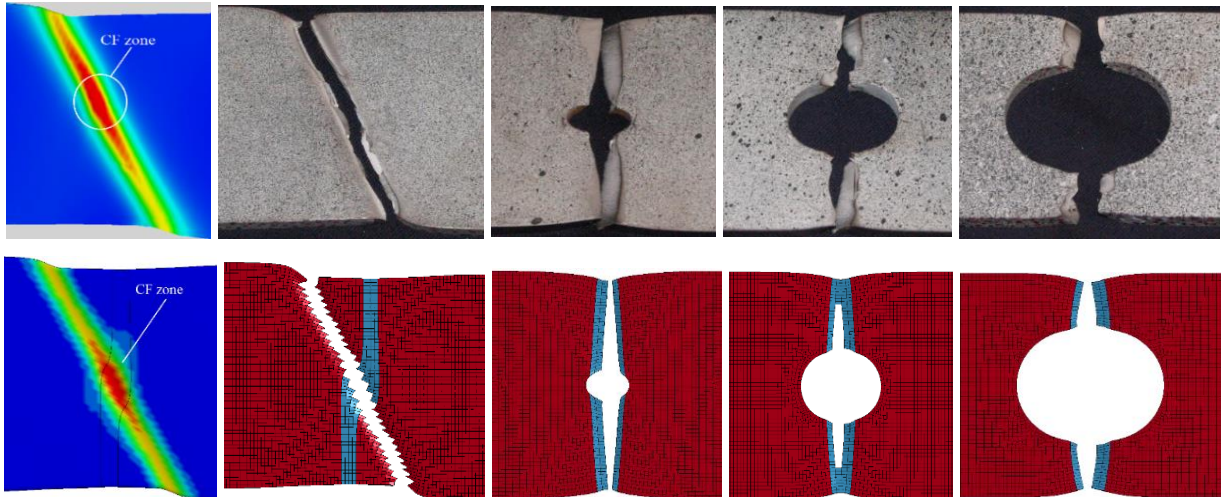


Figure 24. The macroscopic fracture of S960 QC after experiencing HI.

4 CONCLUSION

This investigation has been dedicated to study the effects of fabrication processes on the deformation capacity of S960 UHSS both experimentally and numerically. The generated results lead to the following conclusions:

- The material is highly sensitive towards fabrication processes especially the effects of HI. RCDC of the material can change dramatically after the material experienced heat. According to the findings, the specimen without stress concentration loses 90 % of its RCDC when it has been subjected to HI. The effects of different levels of HI is out of scope of this investigation. However, this could be the subject of another study.
- Presence of stress concentration results in strengthening the specimens after experiencing heat from the point of view of RCDC. Having a hole at FZ results in increasing the stress gradient which increases the plastic deformation at this zone which leads to more deformation capacity before rupture point arrives for SCHAZ and failure of the whole specimen. Increasing the hole-size leads to distribution of stress in a broader area so that the RCDC of the material increases. This has been proven by both FE and laboratory tests.
- Cold forming the material results in decreasing RCDC of the material as well. This specially is revealed at the presence of stress concentration so that increasing the stress gradient decreases the capacity of the material to carry plastic deformations before failure arrives.
- FE simulation based on definition of damage criteria shows a very good correlation with experimental results. According to the numerical simulation results, it is possible to define the effective stress-plastic deformations for each sub zone based on the generated curve for base material without stress concentration with applying some modification. The modifications are based on the changes of Yield and Ultimate capacity of each zone because of hardness changes after fabrication processes.

REFERENCES

ANSI/AISC 360-10. 2013. Specification for structural steel buildings. Third printing. USA: Chicago. 552 p.

Aratani, M., Ishiguro, Y., Hashimoto, Y., Toyoda, S., Kimura, H., Sonobe, O. & Gunji, M. 2013. Development of UTS 980 MPa grade steel tube with excellent formability for automotive body parts. Proceedings of the FISITA 2012 World Automotive Congress, Lecture Notes in Electrical Engineering. pp. 2013-224.

Azhari, F., Heidarpour, A., Zhao, X. L. & Hutchinson, C. R. 2015. Mechanical properties of ultra-high strength (Grade 1200) steel tubes under cooling phase of a fire: An experimental investigation. Construction and Building Materials, Volume 93. pp. 841-850.

Björk, T., Salo, J., Nykänen, T. & Valkonen, I. 2015. On the critical plane of axially loaded plate structures made of ultra-high strength steel. International Institute of Welding (iiw) conference, Helsinki, Finland.

Boyce, B. L. & Dilmore, M. F. 2009. The dynamic tensile behavior of tough, Ultra-high strength steels at strain-rates from 0.0002 s^{-1} to 200 s^{-1} . Int J Impact Eng, Volume 36, No. 2. pp. 263-271.

BS EN 1990:2002. 2002. Eurocode – Basis of structural design. London: BSI. 87 p.

Cadoni, E., Dotta, M., Forni, D., Tesio, N. & Albertini, C. 2013. Mechanical behavior of quenched and self-tempered reinforcing steel in tension under high strain rate. Materials & Design, Volume 49. pp. 657-666.

Cao, K., Guo, Y. J. & Zeng, D. W. 2015. Buckling behavior of large-section and 420 MPa high-strength angle steel columns. Journal of Constructional Steel Research, Volume 111. pp. 11–20.

Cazes, C. & Ronin, F. 2002. Use of HSS1, VHSS2 and UHSS3 steels in the body in white: a panorama of the latest European vehicles, state of art and perspectives. SAE Technical Papers. 8 p.

Dzioba, I., Pała, T. & Valkonen, I. 2013. Strength and fracture toughness of the welded joints made of high-strength ferritic steel. *Acta mechanica et automatica*, vol.7, No. 4. pp. 226-229.

EN 1993-1-12. 2007. Eurocode3: design of steel structures: part 1-12: additional rules for the extension of EN 1993 up to steel grades S700. London: BSI. 9 p.

Feldmann, M., Schaffrath, A. & Schillo, N. 2015. Derivation of new, optimized strength criteria for steel components. Proceedings / METEC & 2nd ESTAD, European Steel Technology and Application Days, Germany: Düsseldorf.

Guo, W., Crowther, D., Francis, J. A., Thomson, A. & Liu, Z, L. L. 2015. Microstructure and mechanical properties of laser welded S960 high strength steel. *Materials and Design*, Volume 85. pp. 534–548.

Guofei, C., Ming, F. S. & Tau, T., M. 2012. Optimized AHSS structures for vehicle side impact. *SAE International Journal of Materials and Manufacturing*, Volume 1. pp. 304-3014.

Hasegawa, K., Kaneko, S. & Seto, K. 2013. Cold-Rolled and Galvannealed (GA) High Strength Steel Sheets for Automotive Cabin Structure. *JFE Technical Report*, No. 18. pp. 80-88.

Kawalla, R. & Waengler, S. 2008. Advanced high strength steels for automotive industry. *Archives of Civil and Mechanical Engineering*, Volume 8, No. 2. pp. 103-117.

LS-DYNA keyword user's manual version R7.1. 2014. Livermore Software Technology Corporation (LSTC). 1206 p.

Lyu, H., Ruimi, A. & M. Zbib, H. 2015. A dislocation-based model for deformation and size effect in multi-phase steels. *International Journal of Plasticity*, Volume 72. pp. 44-59.

Matsuku, S., Hasegawa, K. & Tanaka, Y. 2007. Newly-developed ultra-high tensile strength steels with excellent formability and weldability. *JFE Technical Report*, No. 10. pp. 13-18.

Mukai, Y. 2005. Development of new high-strength steel sheets for automobiles. *SAE Technical Paper*, Volume 1. pp. 1-12.

Nonaka, T., Taniguchi, H., Goto, K. & Yamazaki, K. 2003. Development of ultra-high strength cold-rolled steel sheets for automotive use. *Nippon Steel Technical Report*. pp. 13-15.

Osawa, K., Shimomura, T., Kinoshita, M., Matsudo, K. et al. 1983. Development of High-Strength Cold-Rolled Steel Sheets for Automotive Use by Continuous Annealing. *SAE Technical Paper*. pp. 109-125.

Poorhaydari, K., Patchett, B.M. & Ivey, D.G. 2005. Estimation of cooling rate in the welding of plates with intermediate thickness. *Welding Journal*, Volume 84. pp. 149-155.

Ruukki Oy. 2015. Optim QC structural steels [web document]. [Referred 30.11.2015]. 6 p. Available in PDF-file: <http://www.ruukki.com/Steel/Hot-rolled-steels/Structural-steels/Optim-QC-structural-steels>

Sato, K., Yu, Q., Hiramoto, J., Urabe, T. & Yoshitake, A. 2015. A method to investigate strain rate effects on necking and fracture behaviors of advanced high-strength steels using digital imaging strain analysis. *International Journal of Impact Engineering*, Volume 75. pp. 11-26.

Shaw, J., Kuriyama, Y. & Lambriks, M. 2011. Achieving a lightweight and steel-intensive body structure for alternative powertrains. *SAE Technical Paper*, Volume 1. pp. 1-12.

Solomos, G., Albertini, C., Labibes, K., Pizzinato, V. & Viaccoz, B. 2004. Strain rate effects in nuclear steels at room and higher temperatures. Nucl Eng Des, Volume 229. pp. 139-149.

SSAB. 2009. Welding Handbook. Oxelösund: SSAB Oxelösund AB. 132 p.

SSAB. 2014. Material Certificate Strenx® 960 Tube MH. Helsinki: RUUKKI Metals Oy. 2 p.

SSAB. 2015. Material Certificate Strenx® 960 MC . Helsinki: SSAB Europe Oy. 3 p.

Şükrü, T. 2010. The assessment of carbon equivalent formulas in predicting the properties of steel weld metals. Journal of Materials & Design, Volume 31, Issue 5. pp. 2649–2653.

Turán, P. & Horváth, L. 2015. Experimental behavior of tension plates with center hole made from high strength steel. Nordic Steel Construction Conference, Tampere, Finland.

Verleysen, P. & Degrieck, J. 2004. Experimental investigation of the deformation of Hopkinson bar specimens. International Journal of Impact Engineering, Volume 3, Issue 3. pp. 239-253.

Wallin, K., Pallaspuuro, S., Valkonen, I., Karjalainen, P. & Suikkanen, P. 2015. Fractureproperties of high performance steels and their welds. Engineering Fracture Mechanics, Volume 135. pp. 219-231.